
Direct Numerical Simulation and Analysis of the Flow Field Around a Swept Laminar Separation Bubble

Tilman Hetsch¹ and Ulrich Rist²

¹ Aeronautics and Astronautics, School of Engineering Sciences, University of Southampton, Highfield, Southampton, SO17 1BJ, United Kingdom
`hetsch@soton.ac.uk`

² Institut für Aerodynamik und Gasdynamik, Universität Stuttgart, Pfaffenwaldring 21, 70550 Stuttgart, Germany.
`rist@iag.uni-stuttgart.de`

Summary. The transition process around a short leading-edge separation bubble subjected to a sweep angle of 30° is studied in detail by means of direct numerical simulation, spatial linear stability theory and solutions of the parabolised stability equations. The combined analysis of the averaged flow field, instantaneous flow visualisations and postprocessing data as amplification curves leads to the distinction of four succeeding stages qualitatively comparable to the unswept case. It is shown that the saturation of background disturbances is the key event, after which a rapid breakdown of transitional structures occurs. The mechanism of the final breakdown of this swept scenario of fundamental resonance is best described as an “*oblique K-type transition*”. Great care is taken to isolate and describe of typical structures within each stage as a foundation for the analysis of complex transition scenarios.

1 Introduction

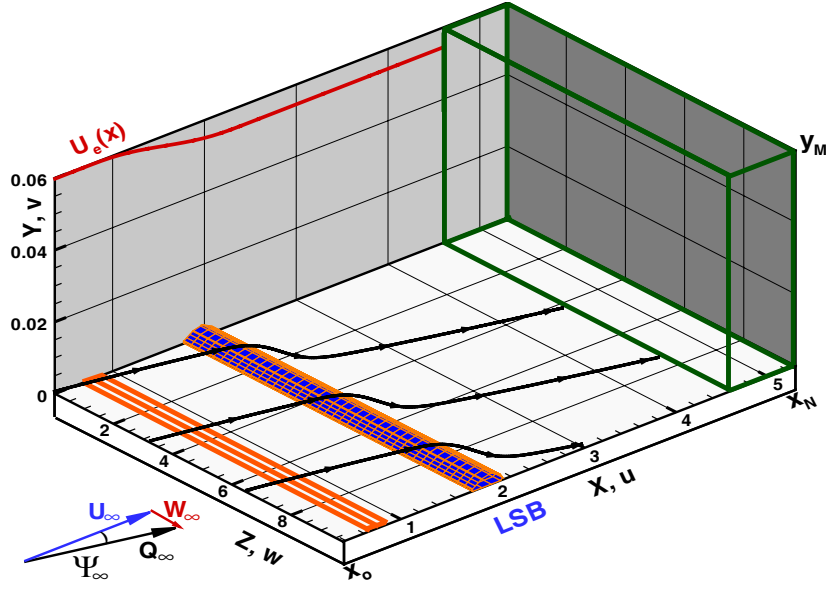
Separation bubbles are observed when laminar boundary layers encounter strong adverse pressure gradients, as on high-lift devices of commercial aircrafts or turbine blades. For instance, a swept separation bubble was measured at a Mach number of 0.245 by Greff [3] on the slat of an Airbus A310-300 in landing configuration. Although most modern passenger airplanes exhibit a sweep angle, research efforts so far have been focused almost exclusively on the easier unswept case. The largest body of experimental data devoted to swept separation bubbles known to the authors was published by Young & Horton [17] and Horton [8] in the late 1960s. Apart from Horton’s benchmark data, literature on swept separation bubbles is still extremely rare. Davis, Carter & Reshotko [2] successfully validated a boundary layer code against Horton’s data and thus confirmed the experiments. More recently, Kaltenbach & Janke

[10] published the direct numerical simulation (*DNS*) of a separation bubble in the flow behind a swept, rearward-facing step. For the lack of literature little is known about the structure, behaviour and the transition mechanisms of swept separation bubbles and especially no systematic picture is established how they can be related to their by now well-investigated unswept counterparts. Note that separation bubbles can be subclassified into laminar or transitional separation bubbles depending on a laminar or turbulent reattachment. This paper is organised in the following way: After a description of the investigated series of swept laminar separation bubbles in section 2 one disturbance scenario is chosen for a detailed analysis in section 3. The aim is two-fold: Firstly it is determined how typical transitional structures express themselves in flow visualisations. This enables us to distinguish a succession of transitional stages in the flow field around a swept laminar separation bubble. Both topics will be addressed in the main subsection 3.4. Before, the disturbance contents of the flow is analysed in subsection 3.1, properties of the averaged flow field are studied in 3.2 and the onset of turbulent flow is discussed in subsection 3.3. Section 4 then describes the *DNS*-codes and the necessary computational resources followed by the conclusions in section 5.

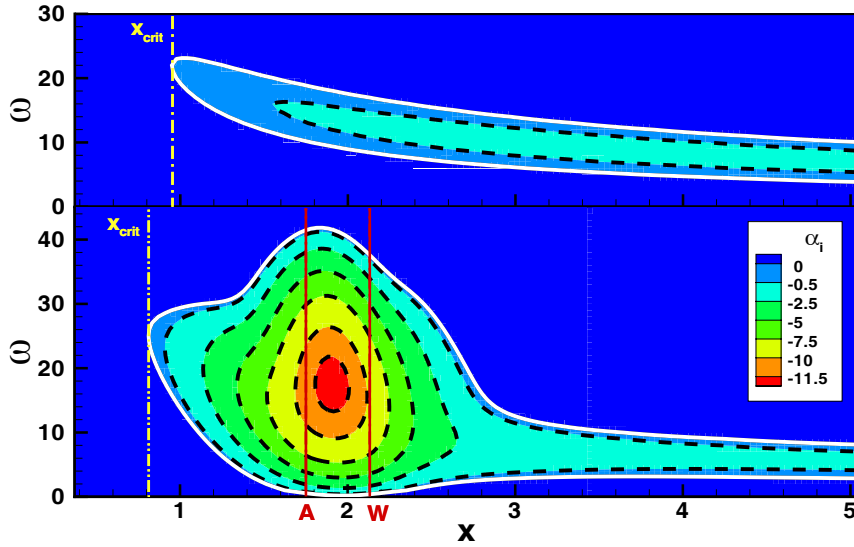
2 Description of the Flow Field

The unswept prototype of the present leading edge bubble was extensively studied by Rist [13] by means of *DNS* and linear stability theory (*LST*). Its extension to swept flows, a verification and validation, as well as the effect of sweep on the base-flow and a *LST* analysis were published in Hetsch & Rist [5]. The reliability and accuracy of *LST* and the parabolised stability equations (*PSE*) in swept laminar separation bubbles were subject of a quantitative investigation in Hetsch & Rist [7]. All *PSE*-results are obtained by the linear version of the code ‘nolot’ of the DLR-Göttingen. It is described by Hein [4], who used the unswept version of the present base flow to prove the applicability of *PSE* to laminar separation bubbles for the first time. Finally, first results about the effect of an increasing sweep angle on the disturbance development in this configuration were reported in Hetsch & Rist [6]. All simulations are split in a *DNS* of the steady laminar base flow Q and a succeeding unsteady *DNS* of the disturbance propagation q' within this base flow. So for any flow quantity $q \in \{u, v, w\}$ the solution takes the form of the decomposition $q(t, x, y, z) = Q(x, y) + q'(t, x, y, z)$.

Only important parameters of the base flow already described in [5] are repeated here: All quantities in the paper are non-dimensionalised by the reference length $\bar{L} = 0.05$ m and the chordwise free-stream velocity $\bar{U}_\infty = 30 \frac{\text{m}}{\text{s}}$, which is held constant for all cases. The x - y - and z -direction are taken normal to the leading edge, wall-normal, and parallel to the leading edge with the associated base flow velocity components U , V and W , respectively. Periodicity is assumed in spanwise direction only, resulting in a quasi-2D base flow



(a) Computational domain with 30° -separation bubble and streamlines. Inflow: Sweep angle Ψ_∞ , freestream velocity Q_∞ with components U_∞, W_∞ . Inside: disturbance strip, dividing streamline Ψ_0 of the bubble. Outflow: schematic sketch of damping zone. Upper boundary condition U_e : potential flow deceleration.



(b) Comparison of *LST*-amplification rates for waves with spanwise wave number $\gamma = 0$ of present flow (bottom) with 30° -‘Blasius’ (top), which results *without* potential flow deceleration. Upstream shift of x_{crit} (point of first disturbance amplification). A: separation, W: reattachment.

Fig. 1. Overview and properties of the present 30° -base flow.

with $(\frac{\partial}{\partial z} \equiv 0)$, but $W(x, y) \neq 0$. The calculation domain shown in figure 1(a) consists of an infinite flat plate subjected to an adverse pressure gradient. The latter is introduced by prescribing a deceleration of the chordwise potential flow velocity $U_e(x)$ at the upper boundary. Different sweep angles Ψ_∞ are realised by varying the spanwise free stream velocity $W_\infty = U_\infty \tan(\Psi)$ and setting $W_e(x) \equiv W_\infty$. Angles are taken with respect to the x -axis throughout the paper. At the inflow located at $x_o = 0.37$ Falkner-Scan-Cooke profiles are prescribed. With a kinematic viscosity of $\bar{\nu} = 15 \cdot 10^{-6} \frac{\text{m}^2}{\text{s}}$ the flow can be characterised by $Re_{\delta_1} = \bar{U}_\infty \bar{\delta}_1(x_o) / \bar{\nu} = 331$, based on the displacement thickness at inflow. The wall-normal coordinate y ranges from 0 to $y_M = 0.238 = 72 \cdot \delta_1(x_o)$. Thus, a family of swept laminar separation bubbles with arbitrary sweep angle is obtained. In agreement with the *independence principle* of incompressible flow discussed in [5] they exhibit identical separation and reattachment positions at $x_{\text{sep}} = 1.75$ and $x_{\text{reat}} = 2.13$, respectively. The steady calculation of the bubbles is justified by its small size and experience with the unswept case in [13]. It was already shown in [7] that the linear stability theory is very accurate in predicting the streamwise wave number α_r . Therefore, the propagation direction Ψ , wavelength λ or phase speed c_r of a disturbance wave

$$\Psi := \arctan(\gamma/\alpha_r), \quad \lambda := 2\pi/\sqrt{\alpha_r^2 + \gamma^2}, \quad c_r := \omega/(\alpha_r^2 + \gamma^2) \quad (1)$$

are based on *LST* throughout this paper, if not stated otherwise. Figure 1(b) displays an overview over the linear stability properties of the 30°-separation bubble in comparison the same flow field *without* the adverse pressure gradient. The presence of the small leading-edge bubble obviously has a remarkable impact on the flow stability: The amplification rates are up to 16 times higher, a much broader frequency-spectrum of disturbances is amplified and the elliptical upstream influence of the separation bubble may be noticed by a shift of x_{crit} , the point where the base flow first becomes unstable.

3 Stages of Transition in a Swept Separation Bubble

For each disturbance scenario a discrete packet of Tollmien-Schlichting (TS) waves is generated by means of suction and blowing through a disturbance strip at $x \in [0.5; 0.64]$. One selected “*primary disturbance*” (*PD*) is excited with an initial amplitude 5 orders of magnitude larger than all other modes. Additionally, 10 low-amplitude “*background disturbances*” (*BD*) with systematically varying spanwise wave numbers $\gamma \in [-50, -40, \dots, 50]$ are introduced as partners for non-linear interactions. As we are interested in scenarios of *fundamental resonance* all waves share the (angular) frequency $\omega = 2\pi(\bar{L}/\bar{U}_\infty)f$ of the primary disturbance. After a initial transient phase steady boundary conditions and periodic wave excitation lead to a quasi-periodic state in time. Together with periodic boundary conditions in the spanwise direction this allows for a double Fourier analysis in time and span in the post-processing. It provides a decomposition of any disturbance quantity q' into

Fourier modes (ω/γ) with amplitudes $\widehat{A}_{(\omega/\gamma)}^q$, from which amplification curves $q'_{(\omega/\gamma)}(x) = \max_y(\widehat{A}_{\omega,\gamma}^q(x, y))$ can be obtained. As modern passenger planes typically exhibit sweep angles of about $\Psi_\infty = 30^\circ$ the disturbance scenario 30° -(20/20) was selected for a detailed analysis of the stages of transition in the flow field around a swept laminar separation bubble. Its primary disturbance showed the greatest disturbance amplification for the sweep angle $\Psi_\infty = 30^\circ$ according to linear stability theory.

3.1 Non-Linear Wave Generation in the Disturbance Spectrum

From the initial disturbance spectrum further disturbances will develop by non-linear mechanisms. Mathematically non-linear wave generation and interaction have their origin in the non-linear convective terms of the Navier-Stokes equations. By studying the multiplication of two Fourier modes it can be shown that any non-linear interaction ' \oplus ' results in the generation

$$(\omega_1/\gamma_1) \oplus (\omega_2/\gamma_2) = \underbrace{(2\omega_1/2\gamma_1) + (2\omega_2/2\gamma_2) + (0/0)}_{\text{autointeraction: } \mathcal{O}(amp^2)} + \underbrace{(\omega_1 \pm \omega_2/\gamma_1 \pm \gamma_2)}_{\text{interaction: } \mathcal{O}(amp_1 \cdot amp_2)},$$

plus its complex conjugate. Each time step every disturbance mode present in the spectrum generates its first higher harmonic and a contribution to the mean flow deformation (0/0). The amplitude of the higher harmonic will be approximately the square-amplitude of its generator. Furthermore, it interacts with every other disturbance by generating the new modes $(\omega_1 + \omega_2/\gamma_1 + \gamma_2)$ and $(\omega_1 - \omega_2/\gamma_1 - \gamma_2)$ with an initial amplitude of approximately the product of those of its generators. Because of the low amplitudes of the background disturbances only *direct* interactions with the primary disturbance will be large enough to contribute to the overall flow development:

$$\underbrace{(20/20)}_{PD} \oplus \underbrace{(20/\gamma)}_{BD} = \underbrace{(40/40)}_{1.HH} + (0/0) + \underbrace{(40/20 + \gamma)}_{TS} + \underbrace{(0/20 - \gamma)}_{CF}. \quad (2)$$

Any background disturbance in the initial spectrum generates therefore a Tollmien-Schlichting wave and a steady crossflow wave (*CF*) with the primary disturbance. With the exception of further higher harmonics of the primary disturbance itself any subsequent interactions of these new modes will again be too small to be of importance. All modes predicted in (2) can be detected in the postprocessing as shown in the amplification curves of figure 2.

3.2 Analysis of the Averaged Flow Field

The direct comparison of the time- and spanwise averaged spanwise vorticity field $[\omega_z] := \Omega_z + (0/0)_{\omega_z}$ with the undisturbed base flow in figure 2 allows the immediate distinction of three zones. However, the deceleration of the

freestream prevents the use of the classical formulas for the boundary layer parameters, which would become misleading and domain height dependant. Following Spalart & Strelitz [15] and Marxen, Lang, Rist & Wagner [12] all boundary layer parameter were determined by the so-called *pseudo velocity* $[u_{pseu}]$:

$$[u_{pseu}](x, y) := \int_0^y [\omega_z](x, \tilde{y}) d\tilde{y} \implies \delta_1(x) = \int_0^\infty \left(1 - \frac{[u_{pseu}](x, \tilde{y})}{[u_{e,pseu}](x)}\right) d\tilde{y}.$$

A preliminary classification of the flow field can now be established as follows: Until $x \approx 1.90$, where the mean flow deformation $(0/0)_u$ reaches about $1.5\% U_e$, no difference to the undisturbed flow appears. As shown in figure 2 the disturbances are still too small to generate a sufficient mean flow deformation to visibly influence the base flow terms of order $\mathcal{O}(1)$. The next zone still resembles the base flow, but distinct differences appear especially in the near-wall region. There, a noticeable rise in the averaged spanwise vorticity $[\omega_z]$ and therefore the wall friction is indicated by an accumulation of isolines and confirmed by figure 3(a). Under the influence of the disturbances the rear part of the separation bubble changes towards a roughly triangle-shaped outline observable in experiments as shown in picture 1.5 in [13]. It also develops the typical pressure plateau displayed in figure 3(a). Qualitatively it compares well with a measured pressure distributions of an unswept transitional separation bubble reported by Lang in figure 3 in [12]. But with the simultaneous saturation of all background disturbances at $x_{sat} = 2.78$ any similarity with the base flow abruptly ends. The hitherto layered structure of the flow switches over to a more chaotic development of the isolines. This is accompanied by a steep rise in the wall friction and the boundary layer thickness δ_{99} . Other indicators also show a shift towards turbulent flow: In the regions of constant $[u_{e,pseu}]$ before and after the separation bubble the shape parameter H_{12} of figure 3(b) can be compared with classical results from Schlichting's book [14] for a two-dimensional flat plate without pressure gradient. It follows from the independence principle that the sweep angle Ψ_∞ will not have a major impact on the comparison. At about x_{sat} H_{12} drops quickly approaching the typical turbulent value of $H_{12} = 1.29$. From the classical theory one can also expect a ratio of $\delta_{99} : \delta_1 = 2.9 : 1$ for a Blasius flow, which is nearly exactly satisfied in the laminar inflow region yielding $2.86 : 1$. The ratio of $8 : 1$ for a fully developed turbulent boundary layer is approached, but not yet reached, towards the end of the domain, where a ratio of $6.8 : 1$ is found at $x = 4.0$. Finally, the velocity profiles in this region are noticeably fuller as compared to the laminar profiles in the first region. Thus after the saturation of the background disturbances a turbulent flow field emerges which quickly approaches the criteria of a fully developed turbulent boundary layer.

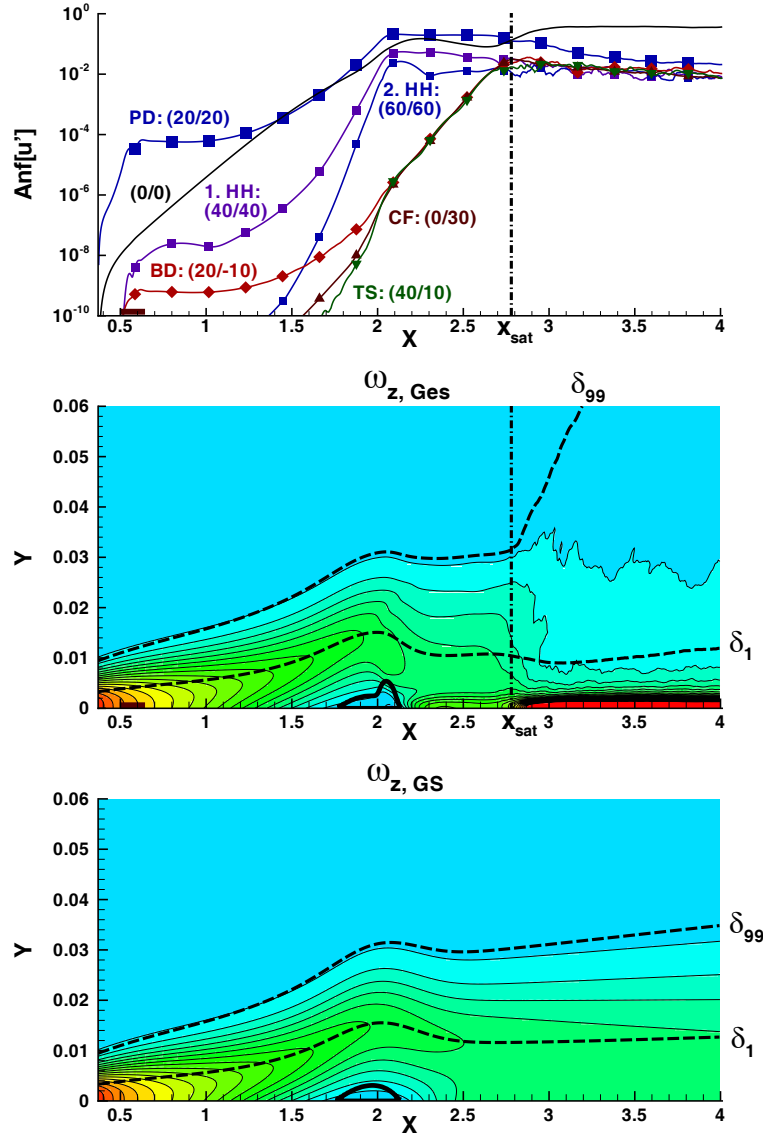
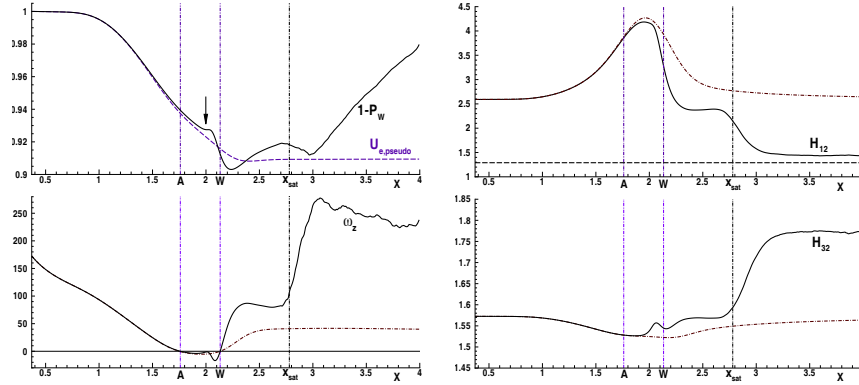


Fig. 2. 30° -scenario with primary disturbance (20/20): Comparison of amplification curves (shown are only the PD , the BD (20/ - 10) and modes directly generated by them, top) with contour plots of the time- and spanwise averaged total flow $[\omega'_z] = \Omega_z + (0/0)\omega_z$, $[\omega'_z] \in [-16.9; 277.5]$: 23 iso-levels $[-45; -35; \dots; 175]$, middle) and the undisturbed base flow ($\Omega_z \in [-5.4; 172.6]$: 23 iso-levels $[-45; -35; \dots; 175]$, bottom). Additionally: The boundary layer thicknesses δ_{99} calculated from $[u'_{pseu}]$ and U_{pseu} respectively and the momentum thickness δ_1 , as well as the saturation position of the background disturbances $x_{\text{sat}} = 2.78$, the dividing streamline Ψ_0 of the separation bubble and the disturbance strip at $x \in \{0.50; 0.63\}$.



(a) Potential flow velocity $u_{e,pseu}$ at upper boundary, pressure plateau (arrow) of $1 - p_w/Re$ of the wall pressure and spanwise vorticity component ω_z there.

(b) Shape parameters H_{12} and H_{32} compared to base flow (dash-dotted). Dashed: $H_{12} \equiv 1.29$, typical for fully developed turbulent boundary layer.

Fig. 3. Properties of the total flow $[q'] = Q + (0/0)_q$ averaged in time and span. The shape parameters were evaluated using u_{pseu} . Vertical lines: $A = x_{sep}$, $W = x_{reat}$, and position of the saturation of background disturbances x_{sat} .

3.3 On the Onset of Turbulence

Although laminar-turbulent transition is a process developing over a certain downstream region in stages, it is sometimes necessary – like in *RANS* calculations – to decide after which point the flow should be regarded as turbulent. According to subsection 3.2 clearly the position of the saturation of the background disturbances x_{sat} should be considered for the present flow. To derive a criterion which yields an exact x -position without interpretation and can thus be programmed for automatic detection, the intersection of the amplification curves of the mean flow deformation $(0/0)_u$ and the primary disturbance was chosen. Physically, this marks the point where the background disturbances have reached a sufficiently high amplitude, such that their combined contribution to the mean flow deformation makes it surpass the primary disturbance as the dominating mode. Just as in figure 2 this point agrees remarkably well with the x_{sat} -position which one would choose on an intuitive level in all investigated scenarios. Furthermore, in disturbance scenarios *without* transition no such intersection occurs. But it should be noted that this intersection is not necessarily unique as also observable in figure 2. In further investigations not presented here the most effective primary disturbance for a given sweep angle was determined by comparison of the ‘earliness’ of the onset of turbulent flow. To this end the above mentioned criterion was deployed. The criterion also seems to work in totally different scenarios like a crossflow-vortex-induced transition published by Wassermann & Kloker, see figure 15 in [16]. Additionally, in the right picture of figure 14 of that publication the background

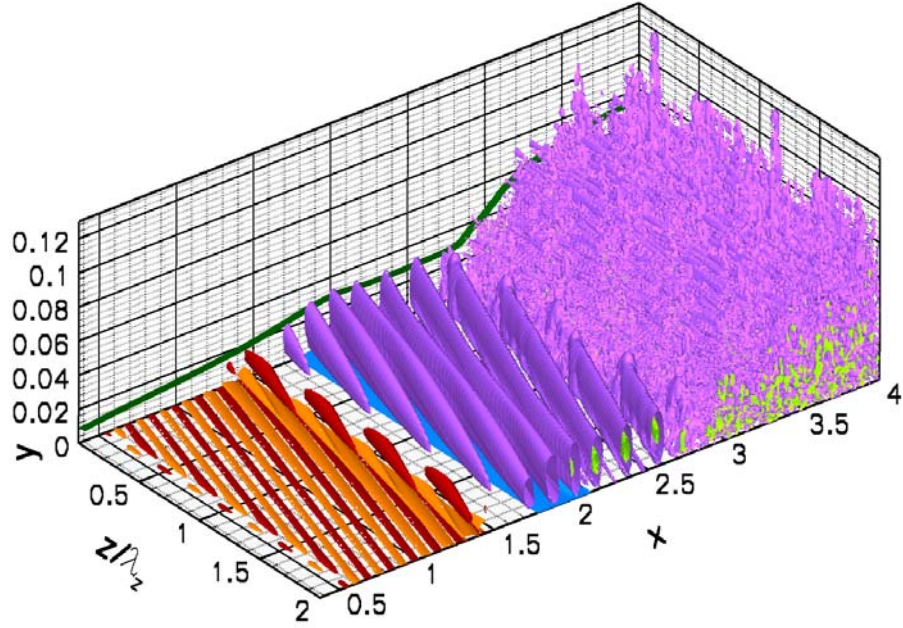
disturbances were switched off. Consequently no transition occurred and the mean flow distortion mainly generated by the dominating vortex could never surpass its generator.

3.4 Characterisation and Properties of the Transition Stages

Figure 4 gives a complete overview over the transition scenario 30° -(20/20) at the end of the 60th disturbance period: Shown are alternating iso-surfaces of the disturbance-component of the spanwise vorticity $\omega'_z = \pm 0.0001$ up to $x = 1.45$ followed by iso-surfaces $\lambda_2 = -1$ and $\lambda_2 = -200$ of the λ_2 -criterion of Jeong & Hussain [9]. Additionally, the boundary layer thickness δ_{99} and the two-dimensional dividing streamline Ψ_0 of the bubble were calculated from data averaged in time and span. The latter is used to visualise the extent of the separation bubble with Ψ_0 defined as the iso-surface $\Psi = 0$ of the stream function $\Psi(x, y) := \int_0^{y^{max}} [u](x, \tilde{y}) d\tilde{y}$. Note that the figure shows twice the spanwise extent, but only the lower half of the actual calculation domain which was moreover cut at the beginning of the damping zone at $x = 4.0$. In order to decompose the overall picture into the different stages of transition, the top view is directly compared with postprocessing data in figure 5:

Stage (I): Linear Disturbance Amplification

One wavelength after the disturbance strip at the latest the boundary layer has filtered out additional disturbance waves of neighbouring wave length which are necessarily co-excited in the process of disturbance generation. Therefore $x = 0.8$ marks the beginning of the *linear domain*, where the growth of any mode can be very accurately described by *LST* and *PSE* as demonstrated in figure 5. At $x_{\text{LinEnd}} \approx 1.91$ the primary disturbances reach an amplitude of $3\% [u_{e,pseu}]$ and the amplification curves depart from the *PSE*-solution. Note that the *LST*-solutions depart earlier at 1.85, so that an investigation with *LST* only would yield a slightly inaccurate smaller linear domain ending with a primary disturbance of $1 - 2\% [u_{e,pseu}]$. As separation occurs at $x = 1.75$, the flow in the front part of the separation bubble can *still* be predicted by linear theories. Throughout stage (I) the primary disturbance dominates other disturbances by 2 – 5 orders of magnitude. Visualisations therefore show this *TS*-wave in its pure form: Its oscillations periodically accelerate and decelerate the base flow profiles creating alternating shear stress at the wall, which in terms is visualised by the ω'_z iso-surfaces. The inclination of their wave fronts of 26° and wavelengths between 0.141 and 0.136 taken from the visualisation 4(b) agree well with its propagation angle $\Psi_{(20/20)}$ in figure 5(b) and its wavelength $\lambda_{(20/20)} = 0.137$ ($\bar{\lambda} = 6.9$ mm) calculated from linear stability theory. As soon as the primary disturbance reaches an amplitude of about $0.1\% [u_{e,pseu}]$ at $x = 1.6$ the first emergence of vortices can be detected by the λ_2 -criterion.



(a) Three-dimensional view: As below twice the spanwise extent is displayed.

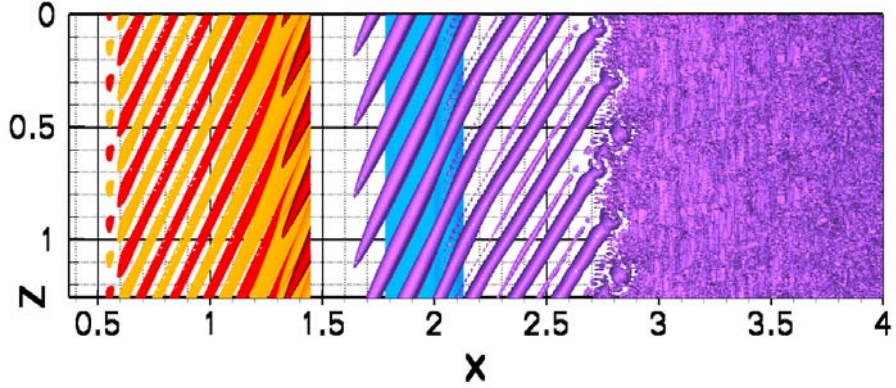
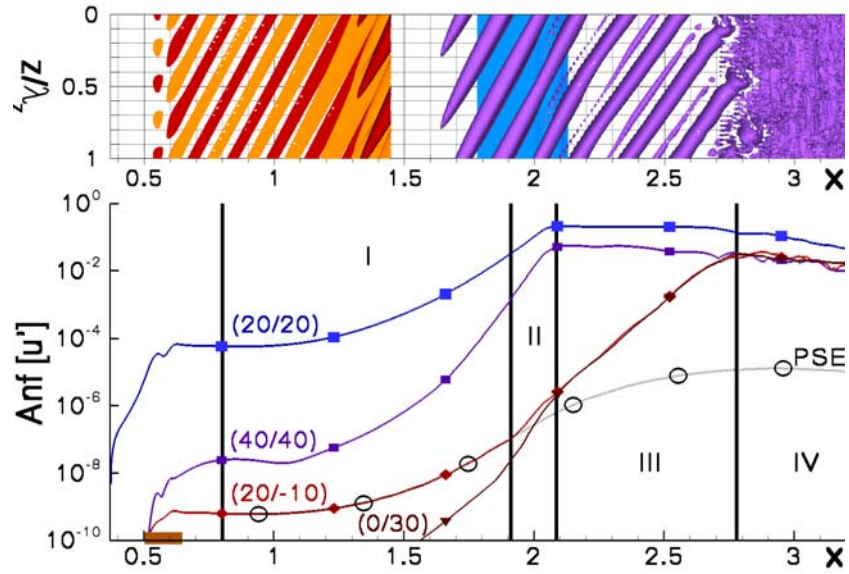
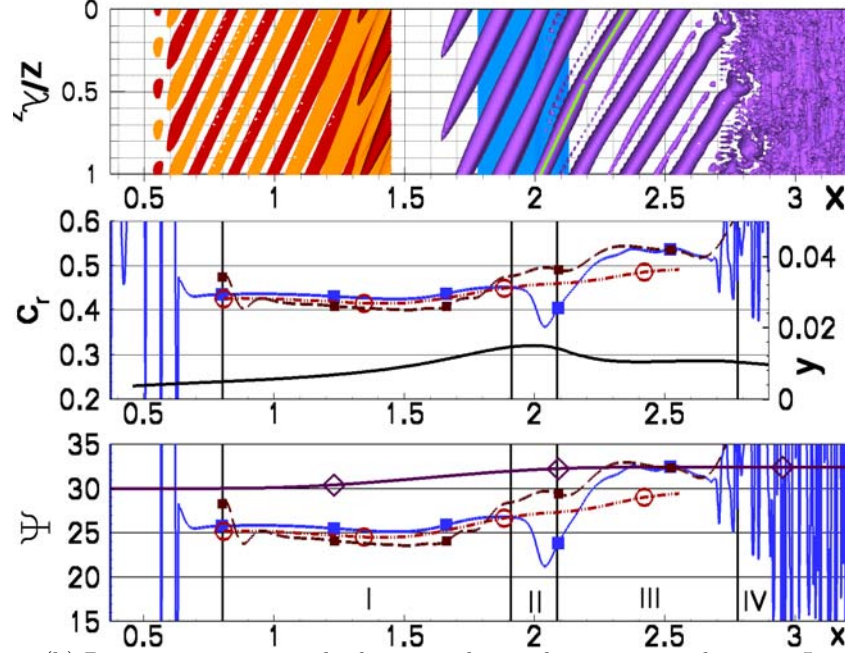
(b) Top view: The x - and z -axis are to scale.

Fig. 4. 3D-visualisation of instantaneous data of the swept transition scenario 30° - $(20/20)$ at the end of the $60th$ disturbance period: Restricted to $x \in [0.37; 1.45]$: ω'_z -iso-surfaces with $\omega'_z \equiv -0.0001$ (red) and $\omega'_z \equiv 0.0001$ (orange). Afterwards: λ_2 -iso-surfaces with $\lambda_2 \equiv -1$ (blue), $\lambda_2 \equiv -200$ (vortex axes, green). From the averaged total flow solution: The dividing streamline Ψ_0 of the separation bubble and the boundary layer thickness δ_{99} (dark green stripe in x, y -plane).



(a) Direct comparison with selected amplification curves from figure 2.



(b) Direct comparison with phase speed c_r and propagation direction Ψ .

Fig. 5. Comparison of the visualisation 4(b) with the most important amplification curves from figure 2 (top) and parameters of the primary disturbance (20/20) (bottom). Bottom: Circle: LST , squares: DNS (large: close to wall, small: freestream), diamonds: Ψ_e . Line without symbol: δ_1 .

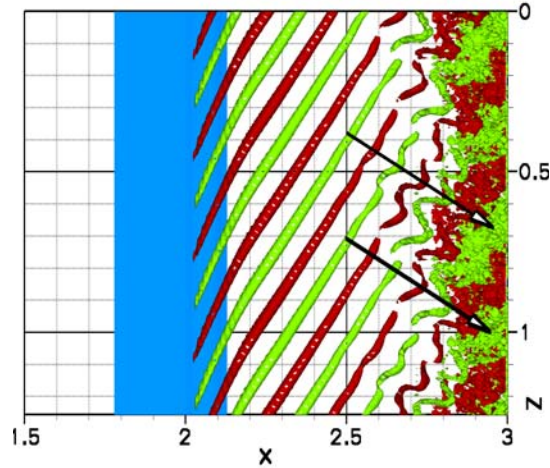


Fig. 6. Close-up on the vortex axes of picture 4(b): Snapshots of λ_2 -iso-surfaces for $\lambda_2 \equiv -200$ at two different instants of time after 59.5 (red) and 60 disturbance periods (green). Arrows: direction of potential flow $\Psi_e(x = 2.5) = 32.4^\circ$.

Stage (II): Secondary Instability

The primary disturbance *continues* to grow according to linear stability theory up to the point of its non-linear saturation. Likewise the dominant structures of the visualisation – vortices with a clockwise sense of rotation – show a smooth changeover from stage (I) to (II). As confirmed by the same angle of inclination as the ω'_z iso-surfaces before and by the absence of other relevant disturbances, they are induced by the high-amplitude primary disturbance only. Higher harmonics play *no* major part in their emergence: Since their generation the higher harmonics of the primary disturbance share the latter's phase speed $c_{r,(20/20)}$. Thus it follows from (1) that $\alpha_{r,(40/40)} = \sqrt{2\omega_{(20/20)}/c_{r,(20/20)} - 4\gamma_{(20/20)}} \approx 2\alpha_{r,20/20}$ and therefore $\Psi_{(40/40)} \approx \Psi_{(20/20)}$, but $\lambda_{(40/40)} \approx \frac{1}{2}\lambda_{(20/20)}$. If the higher harmonics were part of the vortices, a noticeable shortening of the intervals between two vortices in the visualisation would have occurred. Stage (II) naturally ends at $x_{\text{PDsat}} = 2.08$ with the simultaneous saturation of the primary disturbance and its higher harmonics at amplitude levels of 22% $[u_{e,pseu}]$ (PD), 5% $[u_{e,pseu}]$ ((40/40)) and 2% $[u_{e,pseu}]$ ((60/60)). For the respective unswept case Rist [13] has shown that this phase is governed by secondary instability theory. Both cases show a sudden increase of the amplification rates of the background disturbances as a result of their resonance with the primary disturbance.

Stage (III): Coherent Structure of Saturated *TS*-Waves

Sharing a common speed and direction the higher harmonics of the primary disturbance travel together with their generator, which remains unchanged af-

ter their simultaneous saturation. These saturated TS -waves form now a new entity – a *coherent structure* – which massively influences the background disturbances. A description of this coherent structure for unswept separation bubbles can be found in Rist [13]. The presence of the strong vortices formed by the coherent structure forces all background disturbances into a common dependency indicated by an identical growth rate in figure 2, which is slightly damped compared to the steep rise in stage *(II)*. The primary vortices in stage *(III)* are accompanied by weak secondary vortices at their rearward side close to the wall. Such secondary vortices are frequently observed whenever a strong vortex interacts with a wall, reported e.g. at the updraft side of a crossflow vortex in [16]. Particular to the present swept case is a sudden rise in the propagation direction $\Psi_{(20/20)}$ until it *exactly* matches the local freestream direction Ψ_e . Once Ψ_e is reached, $\Psi_{(20/20)}$ stays constant in figure 5(b) up to the final breakup of the coherent structure. According to (1) this rise must correspond to a drop in the streamwise wave number α_r which in turn leads to an increased wavelength $\lambda(x = 2.5) = 8.4\text{mm}$ and a sudden increase of the phase speed c_r by 20%. Both events are visible in the flow visualisations in forms of a larger spacing of the vortices in stage *(III)* and a slight bend in their axes at $x = 2.15$. The presence of the laminar separation bubble complicates this process by stretching the coherent structure: The phase speed development $c_r(PD)$ in figure 5(b) after the separation indicates that the near-wall parts of the vortices are retarded by the presence of back flow while parts above the bubble are locally accelerated due to its displacement. After leaving the bubble both parts share a common rise in c_r and Ψ again. The readjustment of the vortex axes until they are normal to the free stream is therefore an inherent property of the structure, independent of the separation bubble. Stage *(III)* ends abruptly after the saturation of the background disturbances at $x_{\text{sat}} = 2.78$ with the breakdown of the coherent structure. The mechanisms of the breakdown can be clarified by the vortex core lines in figure 6: Viewed in the potential flow direction they display a striking similarity to the classical K -type breakdown of a flat plate boundary layer as described by Bake *et al.* [1]. ‘Spanwise’ modulations along the vortex axes increase downstream until they break the wave fronts apart. The pieces form Λ -vortices which propagate in an aligned fashion exactly in freestream direction. First modulations are observable around $x = 2.6$ where the background disturbances reach amplitudes of 1%. Most likely, this rich spectrum of background disturbances provides the missing ‘oblique’ partners for an *oblique K-type transition*. Moreover, in the present disturbance scenario based on so-called “fundamental resonance” such a transition process can be expected.

Stage *(IV)*: Turbulent Flow

After the breakdown of the coherent structures turbulent flow develops as described in subsection 3.2. Figure 5(a) demonstrates again how well the saturation of the background disturbances coincides with the onset of turbulence.

4 Computational Aspects

4.1 The Algorithms for the Direct Numerical Simulations

Our *DNS*-code solves the three-dimensional Navier-Stokes equations for unsteady, incompressible flow in vorticity-velocity formulation. The quasi-two-dimensional *base flow* equations are discretised with central finite differences of 4th order accuracy. The steady state is reached by the help of a dissipative, semi-implicit, pseudo-temporal ADI approach for the vorticity transport equations. A vectorisable stripe-pattern LSOR technique is employed to solve the Poisson equations for the velocity components. For the *disturbance simulations* a complex Fourier spectral ansatz is used to decompose the flow field in z . Compact finite differences of mostly 6th order accuracy guarantee a highly accurate spatial wave transport and a 4th-order Runge-Kutta scheme is used for the time-stepping. For an in-depth description of the *DNS* algorithms see Wassermann & Kloker [16], from which the present code version differs only in minor details.

4.2 Performance and Computational Resources

For each sweep angle the base flow had only to be calculated once for a highly resolved case with 2786×1537 grid points in x and y to serve for an arbitrary number of disturbance simulations. This can not be parallelised and took 37h user time on a single CPU on the NEC SX-5. The present disturbance scenario – the middle one in table 1 – was a medium sized example of an extensive series with different disturbance contents and sweep angles. As the code was designed for the NEC SX-4/SX-5/SX-6, only one node per run would be requested on the NEC SX-8 with its 8 CPUs calculating different Fourier modes in parallel as micro-tasks with an excellent degree of vectorisation of 99%. In a single run as many disturbance periods in time would be completed as possible within the run-time limit. Afterwards the jobs were restarted until the quasi periodic state was reached. The main advantages of the NEC SX-8 were its speed, the generous amount of main memory and the possibility to work with 3 – 4 different scenarios simultaneously by allocating a node each.

Table 1. Performance data of a small, medium & large run with ‘*Perio*’ disturbance periods per single run out of final number, ‘*time/run*’ user time per single run, so whole scenario finished after ‘*CPU*’ CPU-hours. Further: Grid points in x & y , number of Fourier modes in z , giga-flops/CPU, main memory, vectorisation rate.

| Name | $X \times Y$ | K_{max} | Gflops | GByte | Vect | Perio | time/run | CPU |
|------------|-------------------|-----------|--------|-------|-------|-------|----------|-------|
| 30°-sweep | 2402×273 | 15 | 4.85 | 9 | 99.0% | 24/48 | 110h | 220h |
| 30°-visu | 2402×273 | 31 | 4.89 | 18 | 99.1% | 4/60 | 38h | 570h |
| CF-TS-int. | 3730×545 | 31 | 4.95 | 55 | 99.3% | 2/48 | 145h | 2610h |

5 Conclusions

The stages of laminar-turbulent transition in the flow field around a swept laminar separation bubble have been analysed and visualised in detail. The development of a discrete spectrum of oblique Tollmien-Schlichting waves dominated by a “primary disturbance” of higher amplitude was qualitatively similar to the unswept case: *(I)* Linear disturbance amplification until the primary disturbance reaches a sufficient amplitude of 3% of the local free-stream velocity. Towards the end of this phase vortices induced by the primary disturbance emerge, after its amplitude surpasses 0.1%. *(II)* A stage of secondary flow instability with strong resonance of the background disturbances with the high-amplitude vortices of the primary disturbance, which still grows according to *LST* until saturation at an amplitude level of 22%. Because of the strong amplification rates inside the bubble this phase is quite short, so that secondary instability represents a comparatively unimportant mechanism in separation bubbles in general. *(III)* A coherent structure is formed by the simultaneously saturating primary disturbance and its higher harmonics, which forces any background disturbance into a common dependency indicated by identical amplification rates. The vortices change their orientation until everything evolves exactly in freestream direction. The stage ends with a rapid breakdown immediately after the saturation of the background disturbances. The event is triggered by the breakup of the vortex cores into aligned *A*-vortices, which resemble an oblique *K*-type transition. *(IV)* Emergence of turbulent flow which quickly approaches criteria of a fully turbulent boundary layer. Within all scenarios of fundamental resonance for a sweep angle of 30° the chosen case exhibits the greatest linear amplification of the primary disturbance. Furthermore, it could be shown that the intersection point between the amplification curves of the mean flow deformation and the dominant disturbance marks the saturation of the background disturbances. It is therefore a good indicator for the onset of turbulent flow in different transition scenarios with one dominating disturbance. The interpretation of flow visualisation by direct comparison with postprocessing data within the same figure has been highly fruitful. The knowledge, how typical flow structures express themselves in the visualisations and how such structures develop and interact, provide the “building blocks” for the analysis of more complex disturbance scenarios. To utilise them, a computer aided decomposition of a complex flow field into its elements will be necessary as proposed by Linnick & Rist in [11].

Acknowledgements

The authors would like to thank the DLR-Göttingen and especially Dr. Hein for the possibility to use the linear ‘nolot’-PSE-code. The financial support by the Deutsche Forschungsgemeinschaft (DFG) under contract number RI 680/12 is gratefully acknowledged. All CPU-time for the simulations was provided by the HLRS in Stuttgart.

References

1. S. Bake, D.G.W. Meyer, U. Rist (2002): *Turbulence mechanisms in Klebanoff transition: a quantitative comparison of experiment and direct numerical simulation*. J. Fluid Mech., **459**, pp. 217–243.
2. R. Davis, J. Carter, E. Reshotko: *Analysis of Transitional Separation Bubbles on Infinite Swept Wings*. AIAA Vol. **25**, No. 3, (1987), pp. 421–428.
3. E. Greff: *In-flight Measurements of Static Pressures and Boundary-Layer State with Integrated Sensors*, J. Aircraft, **28**, No. 5, (1991), pp. 289–299.
4. S. Hein: *Linear and nonlinear nonlocal instability analyses for two-dimensional laminar separation bubbles*. Proc. IUTAM Symp. on Laminar-Turbulent Transition, Sedona, USA, Sep. 1999, Springer, pp. 681–686.
5. T. Hetsch, U. Rist (2004): *On the Structure and Stability of Three-Dimensional Laminar Separation Bubbles on a Swept Plate*. In: Breitsamter, Laschka et al. (Eds.): *New results in numerical and experimental fluid mechanics IV: Proceedings of the 13th DGLR/STAB-Symposium, Munich 2002*. NNFM, **87**, Springer, pp. 302–310.
6. T. Hetsch, U. Rist (2006): *The Effect of Sweep on Laminar Separation Bubbles*. In: R. Govindarajan (Ed.): *Sixth IUTAM Symposium on Laminar-Turbulent Transition*, Proc. IUTAM-Symp. Bangalore, India, 2004, Fluid Mechanics and its Applications, Vol. 78, Springer-Verlag, pp. 395–400, 2006.
7. T. Hetsch, U. Rist (2006): *Applicability and Quality of Linear Stability Theory and Linear PSE in Swept Laminar Separation Bubbles*. Proc. of the 14.th DGLR/STAB Symposium. Accepted for publication. To appear 2006.
8. H. Horton (1968): *Laminar Separation Bubbles in Two and Three Dimensional Incompressible Flow*. PhD thesis, Department of Aeronautical Engineering, Queen Mary College, University of London.
9. J. Jeong, F. Hussain (1995): *On the identification of a vortex*. J. Fluid Mech., **285**, pp. 69–94.
10. H.-J. Kaltenbach, G. Janke (2000): *Direct numerical simulation of a flow separation behind a swept, rearward-facing step at $Re_H = 3000$* . Physics of Fluids, **12**, No. 9, pp. 2320–2337.
11. M. Linnick, U. Rist: *Vortex Identification and Extraction in a Boundary-Layer Flow*. In: G. Greiner, J. Hornegger, H. Niemann, M. Stamminger (Eds.): *Vision, Modelling, and Visualization 2005 Proc.* November 16–18, 2005. Erlangen, Germany, Akad. Verlagsges. Aka, Berlin, pp. 9–16.
12. O. Marxen, M. Lang, U. Rist, S. Wagner: *A Combined Experimental/Numerical Study of Unsteady Phenomena in a Laminar Separation Bubble*. Flow, Tub. and Comb. **71**, Kluwer Acad. Pub., 2003, pp. 133–146.
13. U. Rist: *Zur Instabilität und Transition in laminaren Ablöseblasen*. Habilitation, Universität Stuttgart, Shaker 1999.
14. H. Schlichting (1982): *Grenzschicht-Theorie*, 8. Auflage, Verlag G. Braun.
15. P. Spalart, M. Strelets (2000): *Mechanisms of Transition and Heat Transfer in a Separation Bubble*. JFM, **403**, pp. 329–349.
16. P. Wassermann, M. Kloker: *Mechanisms and passive control of crossflow-vortex-induced transition in a three-dimensional boundary layer*. J. Fluid Mech. **456**, Camb. Univ. Press 2002, pp. 49–84.
17. A.D. Young, H.P. Horton (1966): *Some Results of Investigations of Separation Bubbles*. AGARD CP No. 4, pp. 780–811.